Geophysical Journal International

Geophys. J. Int. (2019) **217,** 879–893
Advance Access publication 2019 February 01
GJI Seismology

doi: 10.1093/gji/ggz069

Imaging subsurface structures in the San Jacinto fault zone with high-frequency noise recorded by dense linear arrays

Dimitri Zigone,[1] Yehuda Ben-Zion,[2] Maximilien Lehujeur,[1,3] Michel Campillo,[4] Gregor Hillers[5] and Frank L. Vernon[6]

[1] *Institut de Physique du Globe de Strasbourg, Universite´ de Strasbourg, EOST, CNRS UMR7516, F-67084 Strasbourg, France. E-mail: zigone@unistra.fr*
[2] *Department of Earth Sciences, University of Southern California, Los Angeles, CA 90089-0740, USA*
[3] *Géosciences Environnement Toulouse, Observatoire Midi-Pyrénées, CNRS UMR5563, Université Paul Sabatier, F-31400 Toulouse, France*
[4] *Institut des Sciences de la Terre, Université Grenoble Alpes, CNRS, IRD, BP 53, F-38041 Grenoble, France*
[5] *Institute of Seismology, University of Helsinki,* FI-00014 *Helsinki, Finland*
[6] *Scripps Institution of Oceanography, University of California San Diego, La Jolla, CA 92093, USA*

Accepted 2019 January 31. Received 2019 January 29; in original form 2018 August 30

SUMMARY

Cross-correlations of 2–35 Hz ambient seismic noise recorded by three linear arrays across the San Jacinto Fault Zone (SJFZ) in Southern California are used to derive high-resolution shear wave velocity models for the top 50–90 m of the crust at the array locations. Coherent Rayleigh surface waves are inverted to construct 2-D maps of group velocities in the range 0.2–0.6 km s^{-1}. These maps are inverted to shear wave velocities around the fault using a Markov Chain Monte Carlo approach. The results show marked low-velocity zones in the top 20–30 m with velocity reduction up to 35 per cent and shallow flower structures at depth shallower than 50 m. The derived velocities, location of low-velocity zone with respect to main surface traces and shape with depth are generally consistent with borehole measurements and previous imaging of deeper sections of the SJFZ at the same sites or nearby. The imaging technique requires only ∼30 d of data (90 per cent of the signal-to-noise ratio is obtained in 15 d) and it bridges an observational gap between surface geology and typical tomography studies with no resolution in the top 100 m.

Key words: Seismic tomography; Interferometry; Wave scattering and diffraction; Wave propagation; Wave scattering and diffraction Rheology and friction of fault zones.

1 INTRODUCTION

Tomographic images of fault zones and their surrounding regions provide essential information for many topics including accurate derivation of earthquake locations and source properties, estimations of seismic ground motion and analysis of geodetic data (e.g. Lin *et al.* 2007; Lindsey & Fialko 2013; Kurzon *et al.* 2014). The San Jacinto Fault Zone (SJFZ) is the most seismically active component of the boundary between the North American and Pacific plates in southern California (Hauksson *et al.* 2012; Ross *et al.* 2017). Recent studies derived detailed tomographic images for the region within and around the SJFZ using data recorded by regional stations (e.g. Allam & Ben-Zion 2012; Allam *et al.* 2014; Fang *et al.* 2016; Zigone *et al.* 2015) and linear arrays that cross the SJFZ at different locations (Fig. 1; e.g. Yang *et al.* 2014; Qiu *et al.* 2017; Share *et al.* 2017; Qin et al. 2018). Double-difference earthquake tomography of *P* and *S* traveltimes provided accurate images in the approximate depth range 2–17.5 km (Allam & Ben-Zion 2012; Allam *et al.* 2014), while inversions of Rayleigh and Love wave properties constructed from the ambient noise in the frequency range 0.07–0.33 Hz yielded reliable images in the approximate depth range 0.5–10 km (Zigone *et al.* 2015). A joint inversion of the earthquake traveltimes and surface wave dispersion data provided an integrated velocity model over the approximate depth section 0.5–17.5 km (Fang *et al.* 2016). These regional velocity models were augmented by imaging fault damage zones and bimaterial interfaces based on data recorded by linear arrays (Fig. 1) at different locations (Yang *et al.* 2014; Qiu *et al.* 2017; Share *et al.* 2017; Qin *et al.* 2018).

These studies resolved multiple structural features at seismogenic depths, but they had—like other such studies—essentially no resolution in the top 500 m of the crust. To provide information on local structures at that depth section, several studies analysed ambient noise data at frequencies up to 10 Hz recorded by a dense rectangular array at the Sage Brush Flats (SGB) site of Fig. 1 (Ben-Zion *et al.* 2015; Roux *et al.* (2016) and Mordret *et al.* (2018)). Seismic imaging of the top crust is challenging because of the increased small-scale heterogeneities, produced by multiple deformation processes that are effective at the subsurface (e.g. passing seismic waves, fluid-rock interactions, thermoelastic strain, etc.), and requires high station density to be resolved. Roux *et al.* (2016)

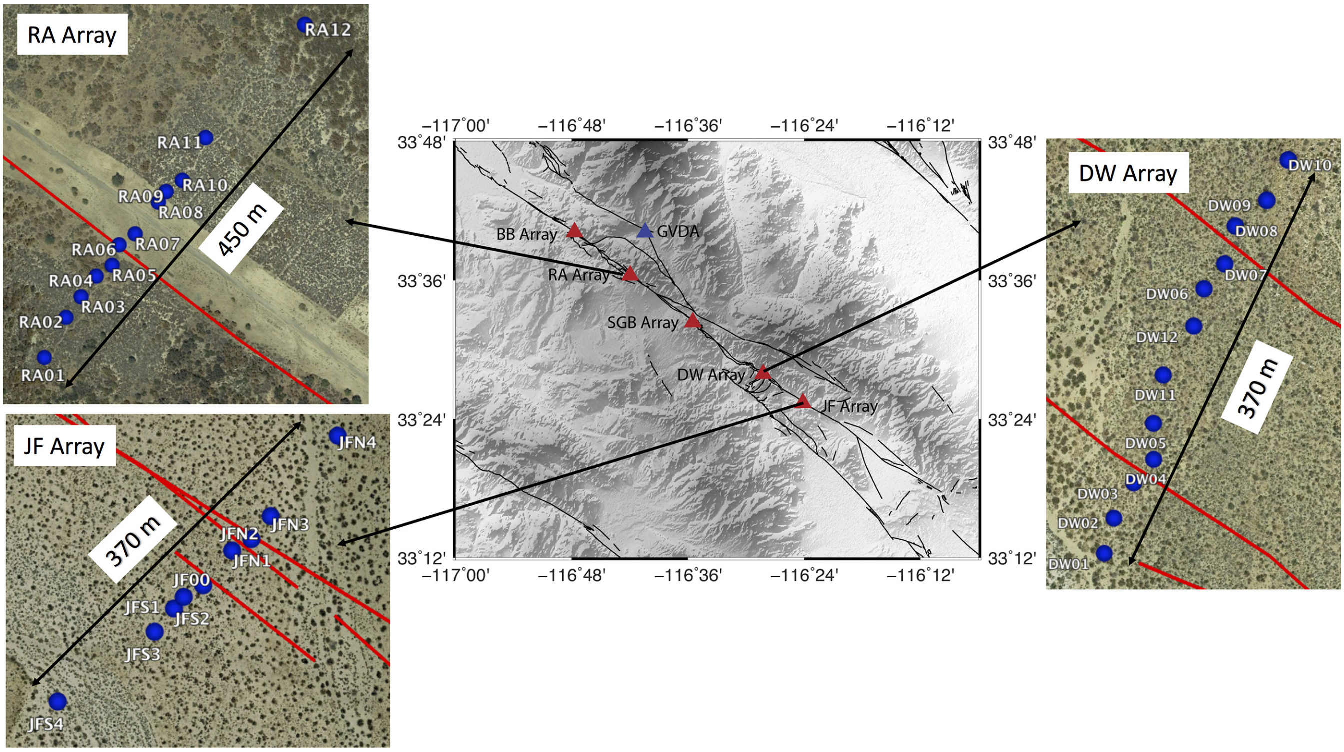

Figure 1. A map of the study area along the San Jacinto fault zone in southern California. The red triangles show locations of across-fault linear arrays DW, JF and RA used in this study. The insets show Google Earth zoom views of each of the three arrays with blue dots marking station locations. The red lines in each inset presents the locations of the surface fault strands based on geological mapping (T. Rockwell, personal communication, 2015). The blue triangle indicates the location of the Garner Valley Downhole Array (GVDA).

and Mordret *et al.* (2018) applied double-beamforming to extract phases from the high-frequency noise recorded by the dense rectangular array and Hillers *et al.* (2016) used a focal spot imaging technique that provided images of the velocity and anisotropy. Developing and implementing additional techniques that can be used to image the subsurface can close an important observational gap and provide information that is highly relevant for various topics including estimates of seismic hazard, effective rheology of the subsurface material and environmental seismology topics such as monitoring landslides, ice sheets, glaciers and hydrological changes (e.g. Larose *et al.* 2015; Lecocq *et al.* 2017).

In this work we use data recorded by three linear arrays located on the Clark Fault branch of the SJFZ. Fig. 1 shows the location of the seismic stations of each array together with the position of the surface fault strands derived from detailed surface geology mapping (T. Rockwell, personal communication; see also Salisbury *et al.* 2012). From northwest to southeast, the Ramona array (RA) is situated in a large alluvial fan, 1200 m southeast from the Hog Lake paleoseismic site (Rockwell *et al.* 2015). The Dry Wash (DW) array is located on alluvium (Fig. 1; Salisbury *et al.* 2012). The Jackass Flat (JF) is located on Quaternary alluvium (Fig. 1; Whearty *et al.* 2017). Salisbury *et al.* (2012) showed that for all three array sites, the last surface rupturing event was the M_w ∼7.3 1800 November 22 event with offsets of ∼3.3 m (RA), ∼2.8 m (DW) and ∼2.4 m (JF). The RA site is also located just southeast of the termination of surface rupture of the M_w 6.9 1918 April 21 San Jacinto (Salisbury *et al.* 2017).

Data from the DW, JF and RA arrays are used here to image the shallow velocity structure from analysis of the ambient seismic noise Rayleigh waves at frequencies up to 35 Hz. The surface waves are inverted for shear wave velocities in the top 100 m with a Markov Chain Monte Carlo (MCMC) approach (e.g. Shapiro *et al.* 1997; Stehly *et al.* 2009; Lehujeur *et al.* 2018). The results reveal shallow flower-shaped damage zones (e.g. Ben-Zion & Sammis 2003) surrounded by heterogeneous structures that complement the deeper fault zone imaging results at these and other array locations mentioned earlier. In Section 2 we discuss the data and pre-processing steps applied to the continuous seismic records. Section 3.1 presents the techniques used to compute high-frequency correlation functions and extract dispersion curves from those cross-correlations. All these methodological steps are illustrated on data of the DW array. Section 3.3 presents corresponding results for the JF and RA arrays. The shear wave velocity inversions and obtained velocity models for the top 100 m of the SJFZ are covered in Section 3.4. Finally, the results are discussed and summarized in Section 4.

2 DATA AND PRE-PROCESSING

We analyse continuous seismic data recorded during a 6-month period in 2014 and 2015 at the RA, DW and JF linear arrays across the Clark branch of the SJFZ (Fig. 1). We use data recorded between Julian days 100 and 280 in 2014 for JF array and between Julian days 180 and 360 in 2015 for DW and RA arrays. The DW array consists of 12 Guralp CMG-40T sensors with instrument spacing between 29 and 52 m and a total aperture of 393 m. The JF is composed of nine Nanometrics T120 broad-band sensors with instrument spacing between 14 and 114 m and total aperture of 371 m. The RA array has 12 Kinematrics Episensor strong motion accelerometers with instrument spacing between 15 and 150 m and total aperture of

460 m. The sampling frequency of all instruments is 200 Hz. Below we show basic characteristics of the data and illustrate the pre-processing steps using example record obtained at the DW array.

Fig. 2 shows a typical 24-hr spectrogram (panel a) with the corresponding time-series (panel b) recorded at station DW03 during Julian day 200 in 2015. The seismic records include local earthquakes that appear as high-energy bursts (see Fig. 2a) and strong, almost continuous, high-frequency (HF) excitations in the range 10–80 Hz. In the time-series these features are reflected by a continuous activity with varying amplitude and numerous spikes of increased energy as around 11 hr UTC (Fig. 2b). Systematic examination of data recorded at other days shows that this HF noise is persistent throughout the year with daily fluctuations involving primarily increased activity during daytime. The sources of this HF excitation are not fully understood and could include air-traffic, car-traffic and train events (Inbal *et al.* 2018; Meng & Ben-Zion 2018). However, the DW and JF arrays are in very remote areas with no significant roads within 10 km of either site. The most likely source of high-frequency noise at the DW and JF arrays are wind-gusts and ongoing low-magnitude seismicity below the array; the RA array could also have local traffic as noise sources. Applying beamforming on data recorded by the dense rectangular array at the SGB site, Ben-Zion *et al.* (2015) identified cultural noise dominant in frequency range 1–10 Hz that may be associated with various anthropogenic sources, and clear local excitation dominating the 20–40 Hz frequency range that is likely associated with small earthquakes below the array. Determination of detailed characteristics and origin of the HF noise in the DW and other linear arrays is beyond the scope of this study. Here we use the HF noise to reconstruct correlation functions up to 35 Hz to image the shallow structure below the linear arrays.

The daily correlation functions are computed using the pre-processing procedure of Poli *et al.* (2012), adapted for regional tomography and seasonal variation studies in southern California by Hillers *et al.* (2015) and Zigone *et al.* (2015). The procedure involves removal of large amplitude transients like earthquakes, whitening in a broad frequency band of 1–90 Hz and amplitude clipping at four times the standard deviation in each window. These pre-processing steps were performed in Zigone *et al.* (2015) on 4-hr windows. Here we reduce the window length to 15 min to better eliminate small local earthquakes, with typical duration of a few tens of seconds, while maintaining large portions of noise data. This modification is needed because the higher frequencies used in this work overlap with excitations by a large number of small earthquakes in the SJFZ (Hauksson *et al.* 2012; Ben-Zion *et al.* 2015). The 15-min window choice maximizes the signal-to-noise ratio (SNR) defined as the maximum amplitude divided by the standard deviation of amplitudes in a noise window in the correlation function.

The daily cross-correlations are stacked for 180 d (between Julian day 180 and 360 in 2015) to remove potential small-scale temporal variations and to increase the overall SNR. As all stations record three component signals, we compute the nine intercomponent correlation functions between the vertical (Z), East (E) and North (N) components. This correlation tensor is then rotated along the interstations azimuth to provide correlation functions between the radial (R), transverse (T) and vertical (Z) components. Fig. 3 displays the correlation tensor filtered between 8 and 16 Hz. The observed pattern has more complexity on all components than those obtained for regional studies in the same region (Hillers *et al.* 2013; Zigone *et al.* 2015). This is especially clear on the mixed transverse terms (ZT, TZ, RT and TR) where scattered energy is present due to complex interactions between the wavefield and the fault damage zone (Hillers *et al.* 2014). The TT component shows Love waves propagating between the array stations at about 0.4 km s^{-1}. The RR, ZR and RZ patterns are dominated by almost symmetric Rayleigh waves travelling between the station pairs at about 0.38 km s^{-1}. In addition to these Rayleigh waves, a clear arrival with high apparent velocity is observed at negative times for some components (e.g. RZ and ZZ). This arrival dominates the ZZ anticausal correlations, with amplitudes three times higher compared to the Rayleigh wave and is discussed in the next paragraph.

Particle motion analysis is used to determine the nature of the arrivals (Fig. 4). The analysis is performed on folded correlation functions, where data at negative times are flipped and stacked with positive times (e.g. Shapiro *et al.* 2005; Verbeke *et al.* 2012). Figs 4(a) and (b) show the folded correlation functions between stations DW01 and DW10 (370 m of interstation distance) for the ZZ and ZR components, respectively, along with the windows used for the particle motion analysis (grey and red areas). The short delay window (Fig. 4c) indicates a longitudinal polarization with an almost vertical incident consistent with a wave propagation upwards. This arrival is likely related to the vertically incident body wave reported for ZZ correlation functions at microseimic frequencies in the same region (Hillers *et al.* 2013). Similar early arrivals have also been reported by Roux *et al.* (2016) at frequencies >1 Hz at the SGB site and are believed to be associated with energy produced by numerous quakes occurring below the array (Ben-Zion *et al.* 2015; Roux *et al.* 2016). The later delay window (Fig. 4d) shows a more elliptical particle motion for the ZZ and ZR correlation functions, which confirms that the near symmetric arrivals in Fig. 3 are Rayleigh waves. In the following we focus the imaging analysis on these Rayleigh waves propagating between the station pairs.

3 RESULTS

Using the Rayleigh waves extracted from high-frequency noise cross-correlations, we image the top 100 m of the crust around the Clark fault (Fig. 1). We first derive group velocity maps, illustrating the procedure with data of the DW array, and then invert the frequency-dependent group velocities to depth-dependent shear wave velocity profiles.

3.1 Rayleigh wave tomography at the DW array

We follow generally the methodology described in Zigone *et al.* (2015) to extract dispersion measurements from the correlation functions and derive group velocity maps, with some modifications needed for the current analysis of HF noise. The frequency–time analysis (FTA) of Levshin *et al.* (1989) is used to measure the dispersion of the reconstructed Rayleigh waves between 2 and 80 Hz. We apply the FTA to both the causal and anticausal parts of the correlation functions for all components of the correlation tensors containing Rayleigh waves (RR, ZZ, ZR and ZR). We first compute the FTA for each signal i independently to obtain a normalized frequency–group velocity diagram $N_i(f, u)$, where f is the frequency and u the group velocity. These frequency–group velocity diagrams are then combined using a logarithmic stacking method (Campillo *et al.* 1996):

$$A_s(f, u) = \prod_i N_i(f, u), \quad (1)$$

where $A_s(f, u)$ is the combined frequency–group velocity diagram. The dispersions are measured on the $[A_s(f, u)]^{(1/i)}$ diagram, which

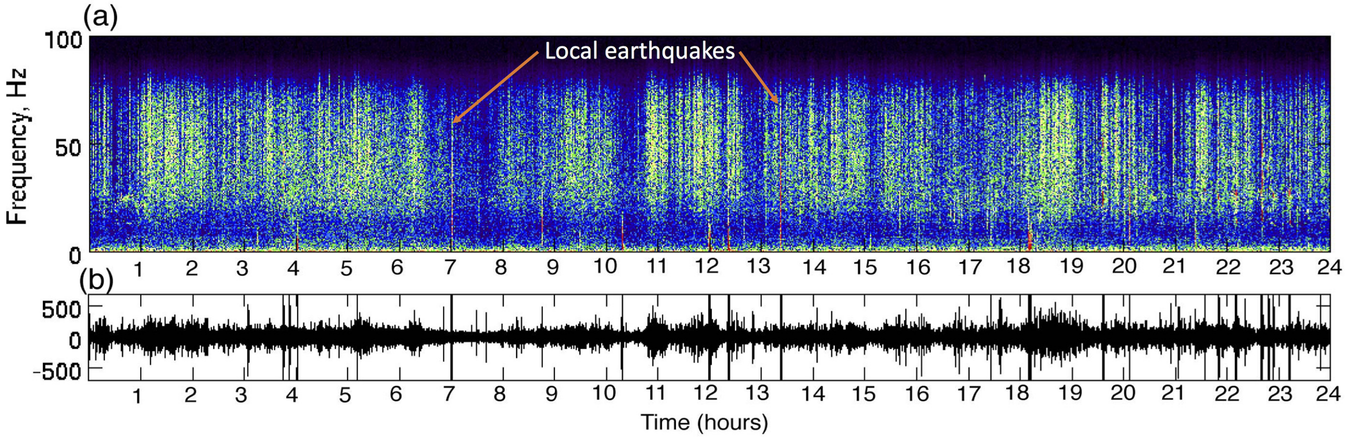

Figure 2. (a) A spectrogram (power spectrum) of the data recorded at station DW03 on Julian day 200 in 2015. Note the high-frequency excitation between 10 and 70–80 Hz. (b) A corresponding time-series bandpass filtered between 1 and 90 Hz.

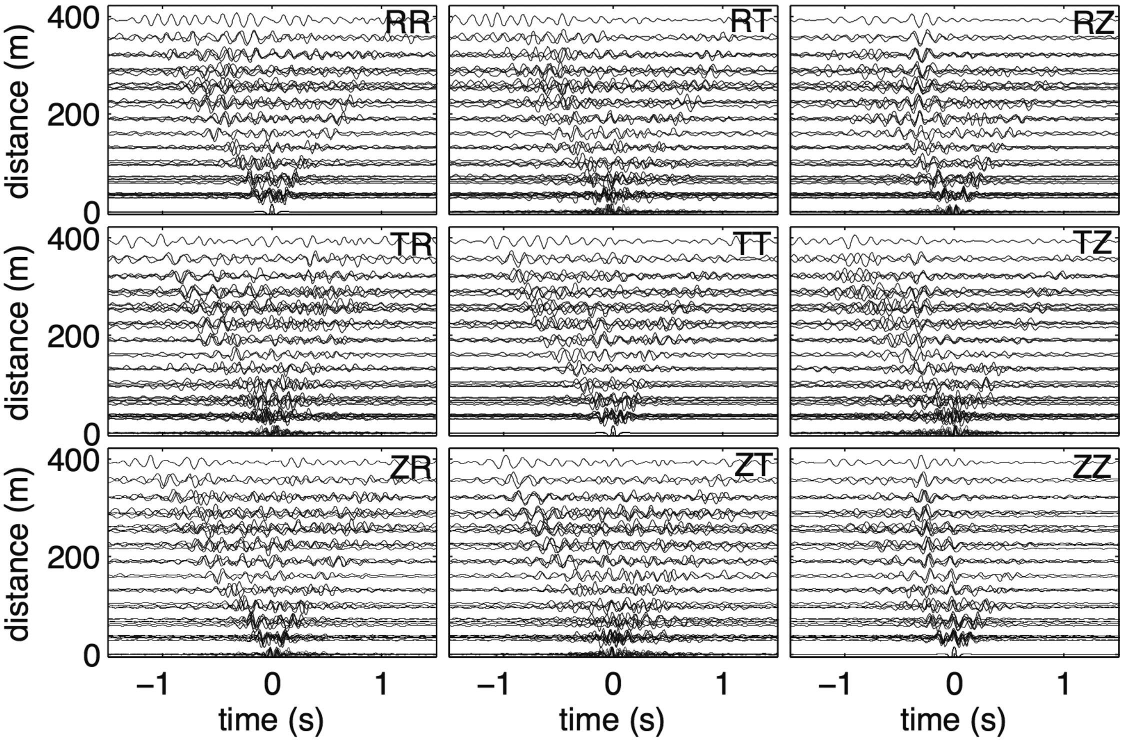

Figure 3. Time–distance plots of correlation functions for the nine components of the correlation tensor. These traces are bandpass filtered between 8 and 16 Hz and normalized by their maximum amplitude per trace. The RR, ZR and RZ traces are dominated by Rayleigh waves, but also contain a vertically incident short delay arrival with moderate amplitude. The ZZ component has the Rayleigh wave but is dominated by arrival with large apparent velocity. The TT component is dominated by Love waves.

provides amplitude values between 0 and 1 independently of the number i of stacked frequency–group velocity diagrams. We use only the frequency–group velocity region on the $[A_s(f, u)]^{(1/i)}$ diagram for pairs of stations that have maximum amplitude above 0.3 (Zigone *et al.* 2015). As explained in Section 2, the ZZ anticausal correlation functions are dominated by short delay arrivals coming from below the array that can bias the FTA results. Therefore, the ZZ anticausal FTA results are discarded from the stacked $[A_s(f, u)]^{(1/i)}$ diagram, giving $i = 7$ in our case instead of the eight possible measurements for Rayleigh waves (ZZ, RR, ZR and RZ on both sides of the correlations). Fig. 5 shows examples of the combined frequency–group velocity diagrams for four pairs of stations along with the extracted dispersion curves (black lines) that will be used in the inversions. We observe clear dispersion with higher group velocity for lower frequencies as expected for Rayleigh waves propagating along the DW array.

To ensure good quality inversions, we require that the measurements meet three criteria: (1) The SNR of the Rayleigh waves should be above 7, (2) for each frequency, paths smaller than one wavelength are excluded and (3) the measured group velocities are fully consistent with the average velocity calculated from the correlation tensor (Fig. 3). Since the number of measurements is relatively small, we visually inspect results associated with all station pairs. Figs 6(a)–(d) present selected paths with corresponding group ve-

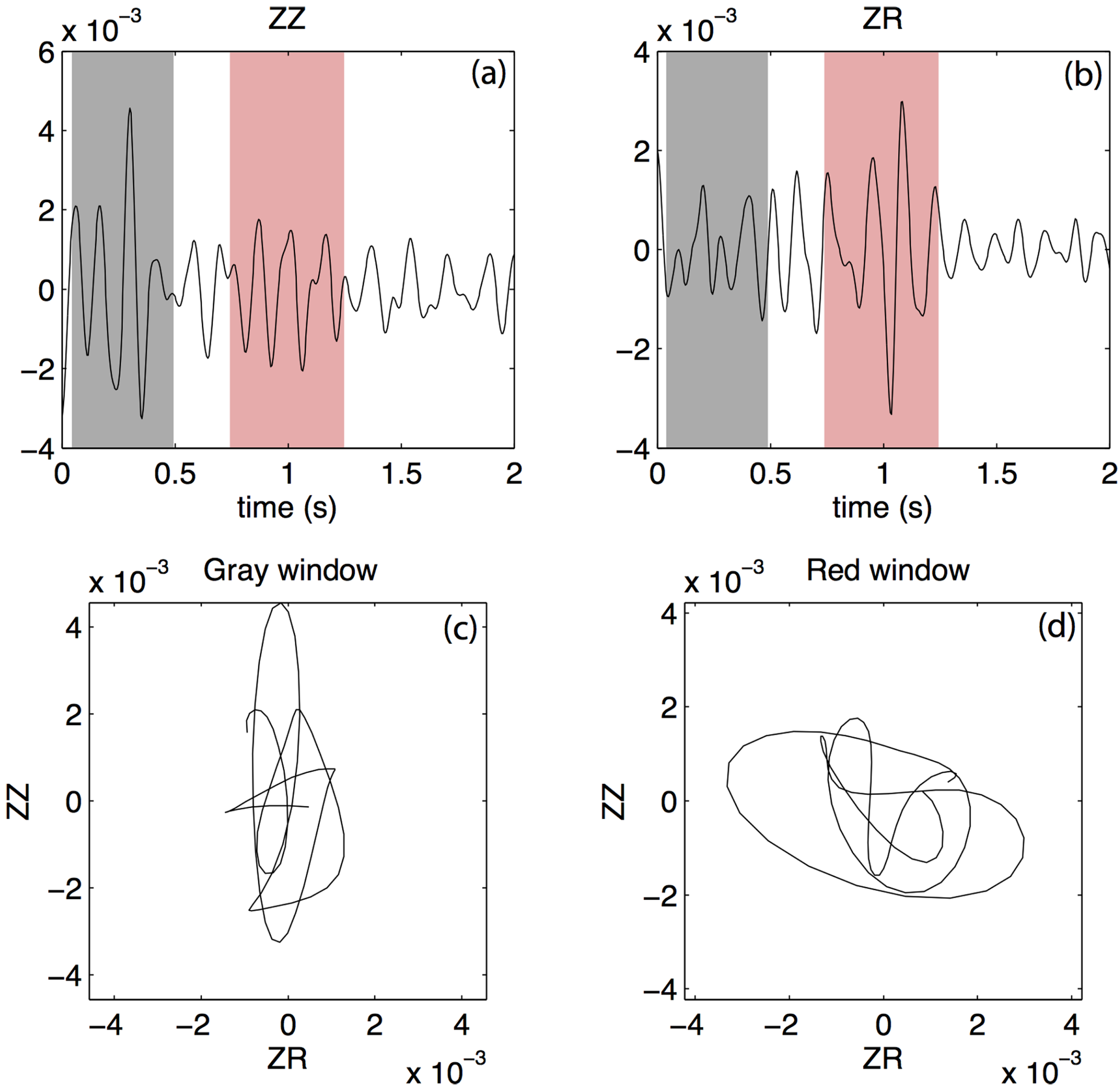

Figure 4. (a,b) Folded ZZ and ZR correlation functions between stations DW01-DW10. The grey and red shaded areas indicate the windows used for the particle motion plots in the bottom panels. The grey window highlights the large apparent velocity arrival visible in ZZ. The red window contains the Rayleigh wave arrival. (c) Particle motion for the grey window. The longitudinal polarization with an almost vertical incident angle indicates a potential body or trapped wave coming from below. (d) Particle motion for the red window with an elliptical polarization characteristic of a Rayleigh wave.

locity measurements (colours) as map views for four different frequencies, 5, 10, 15 and 20 Hz. For all frequencies we observed a reduction of the group velocities for pairs close to station DW12 situated at the centre of the array. This reduction is located between two fault strands (black lines in Fig. 6) and indicates a local shallow damage structure between the two surface traces of the Clark fault. Another reduction of velocity localized around station DW04 appears for frequencies above 15 Hz and is colocated with a southern fault strand plotted in Fig. 6.

To have a better visualization of this damage zone across the fault, we use the Barmin *et al.* (2001) inversion method on a 20 × 20 m grid to compute group velocity maps at different frequencies. The inversion consists of minimizing a linear combination of data misfit, magnitude perturbation and Gaussian spatial smoothing. Four parameters control the regularization of the solution: α and σ control the spatial smoothing while β and λ control the magnitude of the model perturbations. We select the values of parameters through an L-curve analysis (e.g. Hansen & O'Leary 1993; Stehly *et al.* 2009; Zigone *et al.* 2015) where the chosen value is taken near the maximum curvature of the L-curve. Fig. S1 of the Supporting Information shows an example of this selection at 20 Hz giving $\alpha = 0.15$, $\sigma = 30$ m, $\beta = 0.02$ and $\lambda = 0.5$. The number of paths per cell is relatively small in our study, so β has a higher influence on the inversions compared to regional tomography where the number of measurements at each point is much higher (e.g. Stehly *et al.* 2009; Zigone *et al.* 2015).

Figs 7(a)–(d) present the averaged group velocity maps at 5, 10, 15, 20 and 25 Hz. The slight decrease of velocities as the frequencies increase reflects the dispersion of the Rayleigh waves. In addition, we observe clear changes of group velocities across the array for all frequencies. The northeast side of the array from station DW10 to DW06 shows a progressive decrease of group velocities towards the surface trace of the fault. At 5 Hz a clear velocity contrast across the northern fault strand is visible with faster velocity NE of the

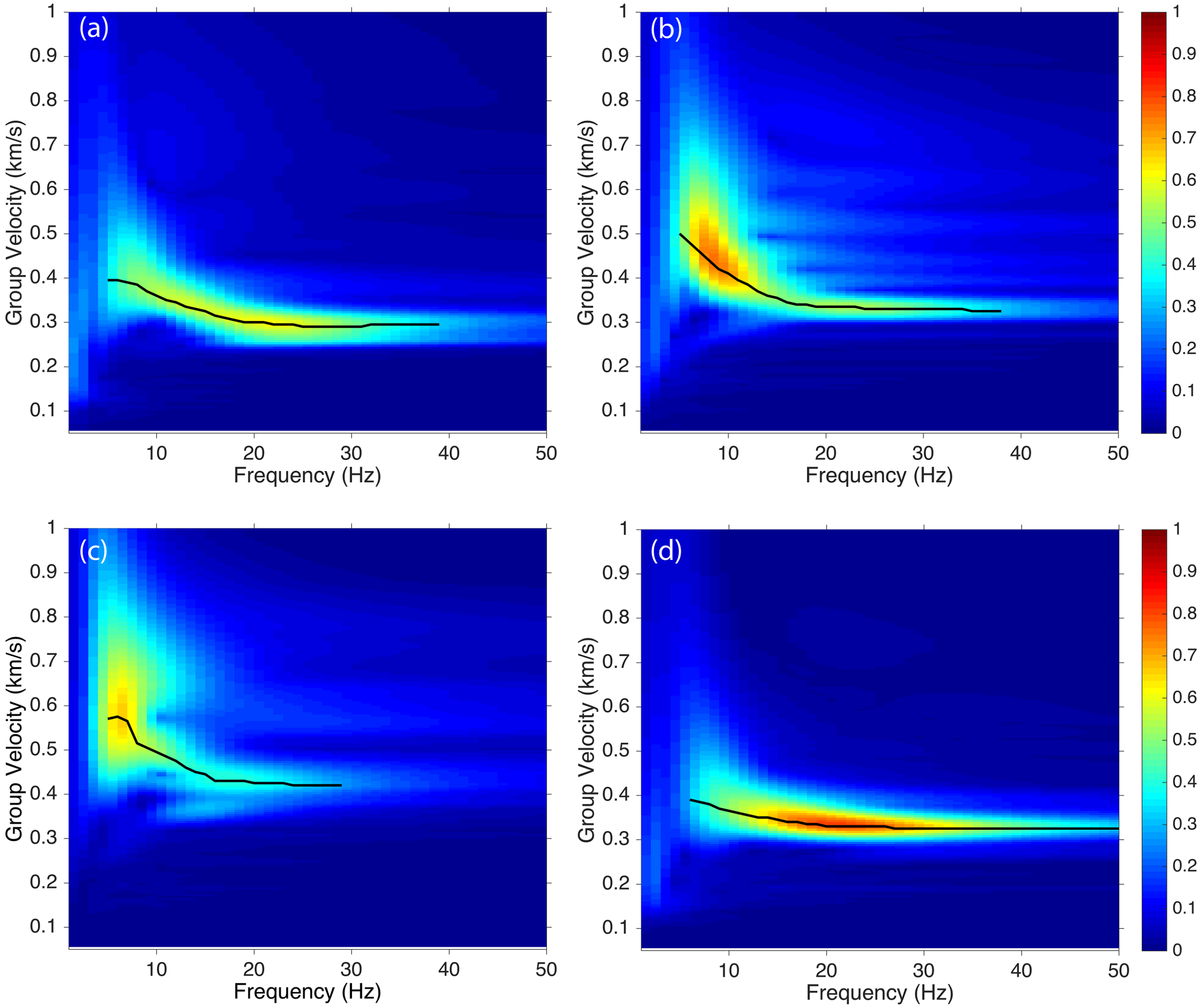

Figure 5. Examples of stacked period-group velocity diagram for (a) DW03-DW05, (b) DW04-DW11, (c) DW07-DW10 and (d) DW11-DW12. The interstation distances are 58, 78, 104 and 30 m, respectively. All examples show frequency-dependent velocities with slower Rayleigh waves as frequency increases. The Rayleigh wave dispersion curves are extracted from these diagrams to image the shallow fault zone structures. The black lines indicate the measured Rayleigh waves dispersion curves and the range where $[A_s(f, u)]^{(1/7)} > 0.3$. For more details, see eq. (1) and the text in Section 3.1.

fault (Fig. 7a). There is a clear reduction in velocities for all frequencies between stations DW12 and DW06 that is located between the two fault strands. This reduction is more pronounced for higher frequencies with velocities down to 0.27 km s^{-1} at 25 Hz. A second low-velocity zone appears near station DW04 for frequencies above 15 Hz and is collocated with the southern fault stand (Fig. 7c–e). The southwest section of the array corresponding to stations DW01 to DW03 presents higher velocities around 0.4 km s^{-1} up to 0.47 km s^{-1} depending on the frequency.

3.2 Resolution

The resolution of the inversions with the Barmin *et al.* (2001) method is controlled by the array geometry and model parametrization. We evaluate the resolution using both the paths density and the resolution matrix to provide the number of measurements and the resolution length at each point of the model. The resolution length is defined as the distance for which the value in the resolution matrix decreased by a factor of two (Barmin *et al.* 2001). Figs 8(a) and (b) present, respectively, the path density in each 20 × 20 m cell and the resolution length for the group velocity map at 20 Hz (see Fig. 7d). As the number of stations is relatively small, the number of measurements varies significantly from cell-to-cell with path densities between 1 and 7. Cells with the smallest number of measurements are located at the edges of the array whereas most cells located between two stations have a path density above 3. The resolution lengths indicate typical resolution in the range of 40–60 m for most cells. Only three cells located at the edges of the array (blue cells on Fig. 8b) have resolution larger than 70 m. The average resolution length over all cells for DW array at 20 Hz is 51.8 ± 15.85 m.

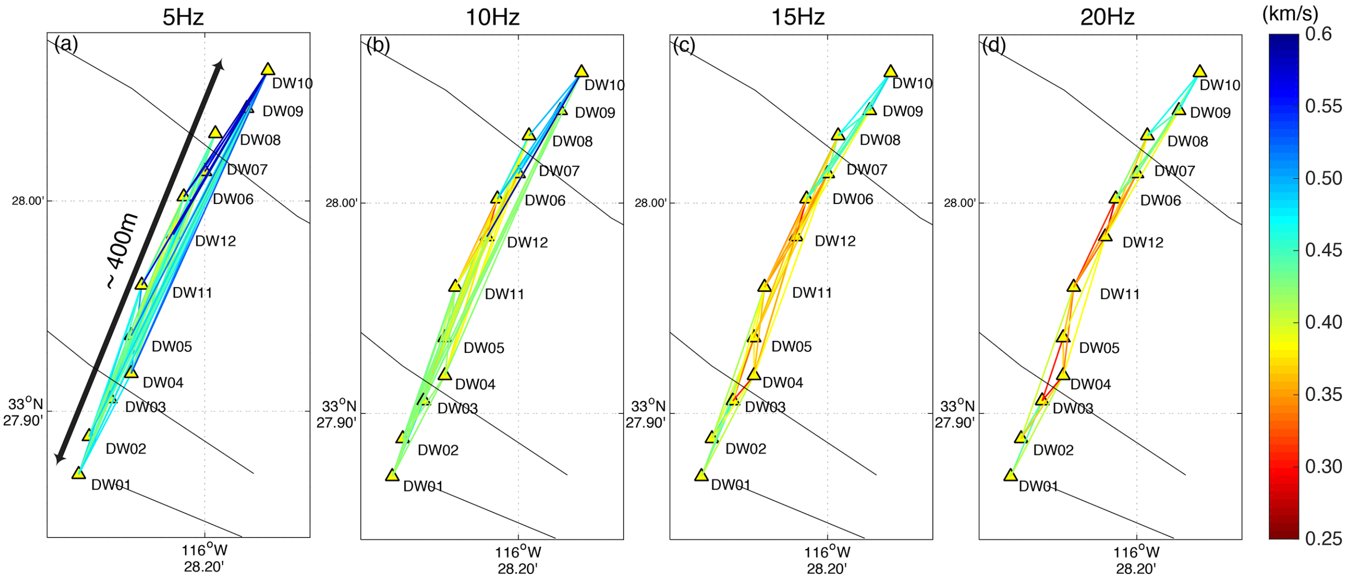

Figure 6. Map views of selected paths at (a) 5 Hz, (b) 10 Hz, (c) 15 Hz and (d) 20 Hz with Rayleigh wave group velocities indicated by colour. The aperture of the array is $\sim$400 m. Note the reductions of velocity around stations DW12 and DW04 in (c) and (d). The solid black lines present the surface traces obtained from detailed surface geology work (T. Rockwell, personal communication, 2015).

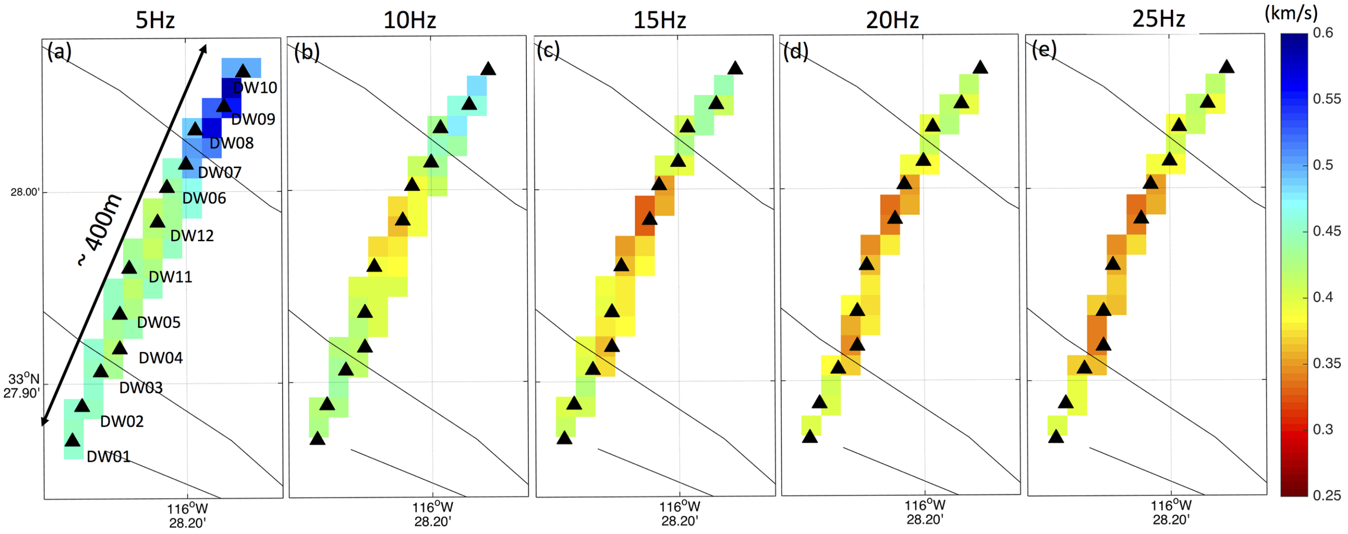

Figure 7. Rayleigh wave group velocity maps at (a) 5 Hz, (b) 10 Hz, (c) 25 Hz, (d) 20 Hz and (e) 25 Hz with Rayleigh wave group velocities indicated by colour. The black triangles are the stations. The solid black lines present the surface traces obtained from detailed surface geology work (T. Rockwell, personal communication, 2015). Note the velocity reductions of velocity around stations DW12 and DW04.

3.3 Along-strike variations

Here we apply similar techniques to seismic records from the RA and JF arrays that cross the SJFZ northwest and southeast of the DW array, respectively (Fig. 1). The results at the DW and JF arrays are based on the frequency range 2–35 Hz, while the results for RA array are associated with a frequency range 8–35 Hz due to the different sensor type (Kinemetrics strong motion Episensor accelerometer, see Section 2). Figs 9(a) and (b) show the group velocity maps at 20 Hz for the two arrays. As observed for DW array (Fig. 8), clear velocity reductions are correlated with the surface traces of the fault, visible between station pairs RA06-RA07 and JFN1-JFN3 (Fig. 9). This and related results by Ben-Zion *et al.* (2015), Hillers *et al.* (2016) and Mordret *et al.* (2018) for the SGB site confirm the systematic presence of a shallow localized damage zone below the surface fault strands for different array locations. However, details of the geometry and velocity reductions change for different locations. This is shown in Fig. 10 with cross-sections of 20 Hz group velocities at the DW, JF and RA arrays, with the origin at the main surface fault traces.

There are several interesting observations in Fig. 10. First, the absolute values of the Rayleigh waves group velocities vary between the arrays. The average velocity across the DW array is $\sim$0.38 km s^{-1}, while those for JF and RA are $\sim$0.3 and $\sim$0.29 km s^{-1}, respectively. As mentioned, all three array sites are located on alluvium sediments. The DW site has alluvium with $\sim$10 m depth over bedrock near the fault and shallowing towards the northeast based on the topography of the site. Using similar arguments, the RA and JF sites are both estimated to have $\sim$100 m of alluvium near the fault trace and shallowing towards the northeast.

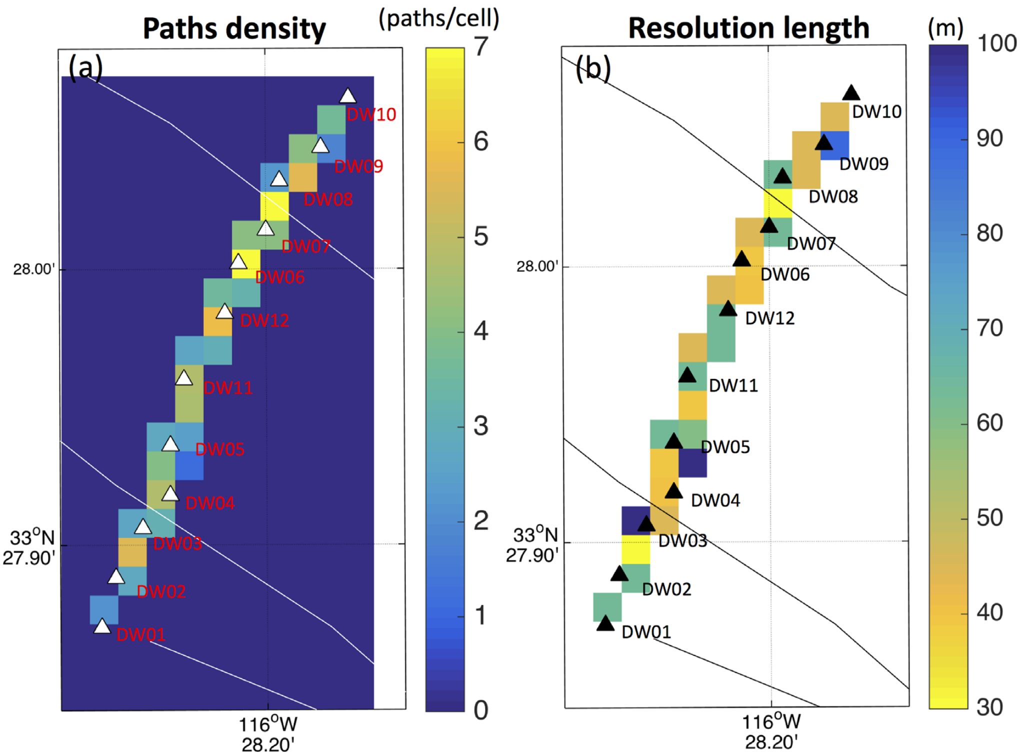

Figure 8. (a) Number of paths per cell for DW array at 20 Hz. (b) Value of the resolution length for DW array at 20 Hz. The average resolution length over all cells is 51.8 ± 15.85 m.

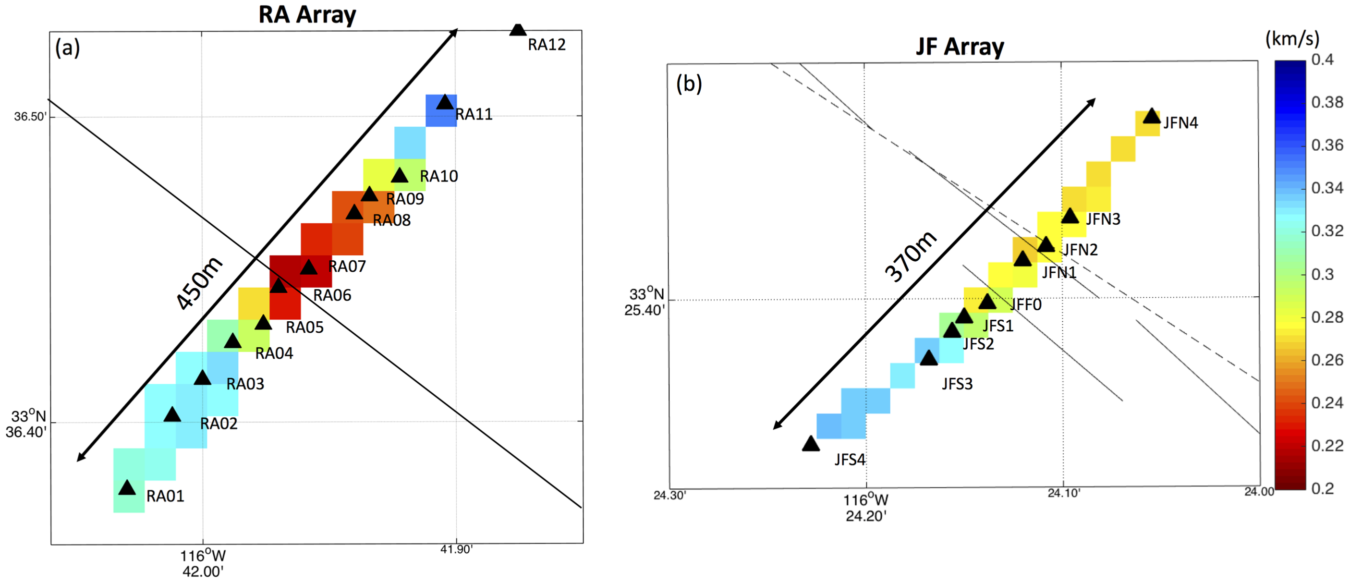

Figure 9. Rayleigh wave group velocity maps at 20 Hz for the (a) RA and (b) JF arrays. The Rayleigh wave group velocities and stations are indicated by colour squares and black triangles, respectively. Note the reductions of velocity around stations RA06-RA08 and JFN1-JFN3. The solid and dashed black lines mark local surface fault traces (T. Rockwell, personal communication, 2015).

This can explain the higher average velocity observed at DW. At the RA site there is a shallow low-velocity zone (LVZ) centred on the main fault strand. The DW site has an LVZ between the two major fault strands and has also a secondary LVZ about 190 m on the SW (left) colocated with the southern fault strand. The reduction of the Rayleigh group velocities at the DW array is ∼18 per cent in the LVZ compared to the velocity at the edges of the array. The RA site has stronger velocity reduction compared to DW and JF with Rayleigh group velocity changing from ∼0.27 km s^{-1} near the fault to ∼0.33 km s^{-1} 100 m away from the fault. The velocity increase is more marked on the southwest side of the fault with ∼0.1 km s^{-1} increase in only 50 m. In contrast, the shallow structure at the JF array is associated with a clear velocity contrast between the SW and NE sides of the fault. This is consistent with observations of local head waves associated with shallow structure at that location (Qiu *et al.* 2017).

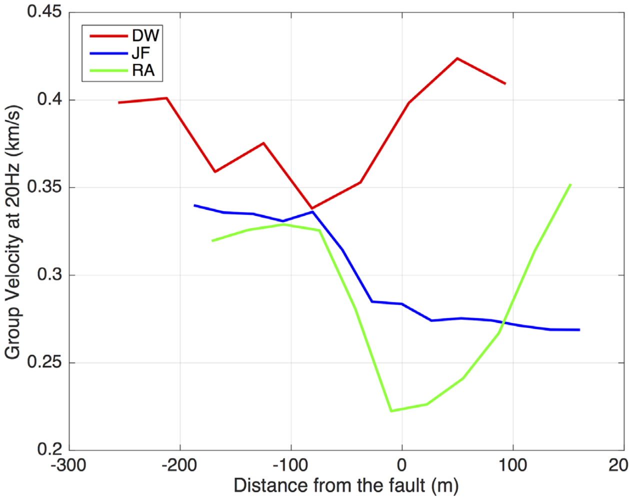

Figure 10. Cross-sections of Rayleigh wave group velocities at 20 Hz as a function of distances relative to the main surface fault trace for DW (red), JF (blue) and RA (green) arrays.

These results show clear along-strike variations of the shallow internal damage zones around the SJFZ, which possibly reflect the different faulting behaviour in the different locations. The simpler Anza section (RA array) has a pronounced damage zone located on the fault with rapid velocity recovery away from the fault. In contrast, the DW and JF arrays in the complex trifurcation area show more smeared shallow damage zones with less variations across the surface fault traces.

3.4 Inversions for shear wave velocities

In this section we use the derived group velocity maps between 2 and 35 Hz to extract a dispersion curve for each cell of the model. These dispersion observations are inverted independently at each location of the maps to obtain depth-dependent shear wave velocity (*Vs*) profiles across the SJFZ at the array's locations. The inversions are done with an MCMC approach which can solve nonlinear inverse problems with non-unique solutions (e.g. Sambridge & Mosegaard 2002; Shapiro & Ritzwoller 2002; Socco & Boiero 2008; Gallagher *et al.* 2009; Maraschini & Foti 2010). We use a parametrization with six layers over a half-space and invert for the *S*-wave velocity and depth of each interface. Since the computation of the surface wave dispersion curves further require a *Vp*/*Vs* and a density model, we also invert for these parameters in each layer, although the sensitivity of group velocity dispersion curves to them is generally low (Xia *et al.* 1999). The likelihood of each model (i.e. the posterior probability density of the model space) is computed as a combination of prior density functions of both model and data spaces (Tarantola 2005).

$$llk\,(m) = \log \rho_M\,(m)\; + \log \rho_D\,(g\,(m))\,, \qquad (2)$$

where *llk* is the logarithm of the likelihood, *m* is an array corresponding to a sample of the model space, ρ_{M} is the prior probability density function (PDF) of the model space, ρ_{D} is the PDF of the data space and *g* is the theory function used to compute dispersion curves.

The prior PDF of the model space ρ_{M} is defined as the product of uniform PDFs on each parameter of the model. Each parameter of the depth inversion is constrained to a uniform range (Table 1) to exclude unrealistic models from the search domain. The prior constraints on the shear wave velocity and *Vp*/*Vs* in each layer are selected using borehole data at the Garner Valley Downhole Array (GVDA) site (Fig. 1). Although these values are taken from one site, the allowed variations account for realistic variations of properties at different locations. In each layer, *Vs* is allowed to vary from 0.1 to 1.5 km s^{-1} (Bonilla *et al.* 2002) and *Vp*/*Vs* can range from 3 to 4 to account for the existence of partially consolidated and heavily damaged material at the subsurface (e.g. Mavko *et al.* 2009). The prior PDF of the data space ρ_{D} is approximated using lognormal probability laws for each point in the dispersion curve. These laws are centred on the velocities derived from the dispersion maps, and we assume that the dispersion points are independent (i.e. the covariance matrix on the data space is taken diagonal; Tarantola 2005). The forward modelling of the dispersion curves for each possible model is done with the program by Herrmann (2013). For each cell we run eight independent Markov chains in parallel in which the step from one model to the next is governed by a Gaussian proposal PDF with a diagonal covariance matrix. The terms of that covariance matrix are adjusted along the inversion to stabilize the acceptance ratio around 25 per cent. Each chain runs until 1000 models have been accepted. In total the inversion keeps about 8000 models over the 32 000 tested for each depth profile. From those 8000 models, the median of the 1000 best models is taken as the solution of the inversion.

Table 1. Prior boundaries of the uniform probability distributions used for each parameter in the assumed layered model.

Layer number	Top depth range (m)	*Vs* range (km s^{-1})	*Vp*/*Vs* range	Density range (g cm^{-3})
1	1–5	0.1–1.5	3–4	2–2.5
2	5–10	0.1–1.5	3–4	2–2.5
3	10–25	0.1–1.5	3–4	2–2.5
4	25–50	0.1–1.5	3–4	2–2.5
5	50–75	0.1–1.5	3–4	2–2.5
6	75–100	0.1–1.5	3–4	2–2.5
Half-space	–	0.1–1.5	3–4	2–2.5

Fig. 11 presents results for an example pixel of the map along the DW array. The black and white curves show the 1000 best models produced by the inversion and the blue curve shows the median, which is the discussed final model. The obtained *Vs* models are well defined with a limited variability within the allowed range (Fig. 11a), and the synthetic dispersion curves fit well with the observed dispersion curves (Fig. 11d). The 1000 best depth profiles obtained for *Vp*/*Vs* and density are uniformly distributed between the imposed boundaries in all inversions (Figs 11b and c) because of the low sensitivity of Rayleigh wave velocities to these parameters (e.g. Xia *et al.* 1999). The 1-D *S*-wave velocity models obtained in every pixel are combined to form a shear wave velocity profile across the fault for each array (Figs 12 and 13). The hatched zones correspond to poorly resolved depths, for which the average variability of the models in Figs 12 and 13 becomes similar to the observed variations of shear wave velocity. The resolved depths vary between the arrays (92 m for DW, 73 m for JF and 45 m for RA) because of the different frequency ranges used at each array along with the varying uncertainties in the group velocity maps. The results for each array are briefly discussed below and are summarized in Table 2.

DW Array: Fig. 12(a) presents shear wave velocities across the DW array. We observe a clear LVZ in the top 15–20 m with a minimum velocity *Vs* ~0.3 km s^{-1} close to station DW12. The low-velocity zone is approximately symmetric around the midpoint between stations DW11 and DW12, as observed with the 20 Hz group

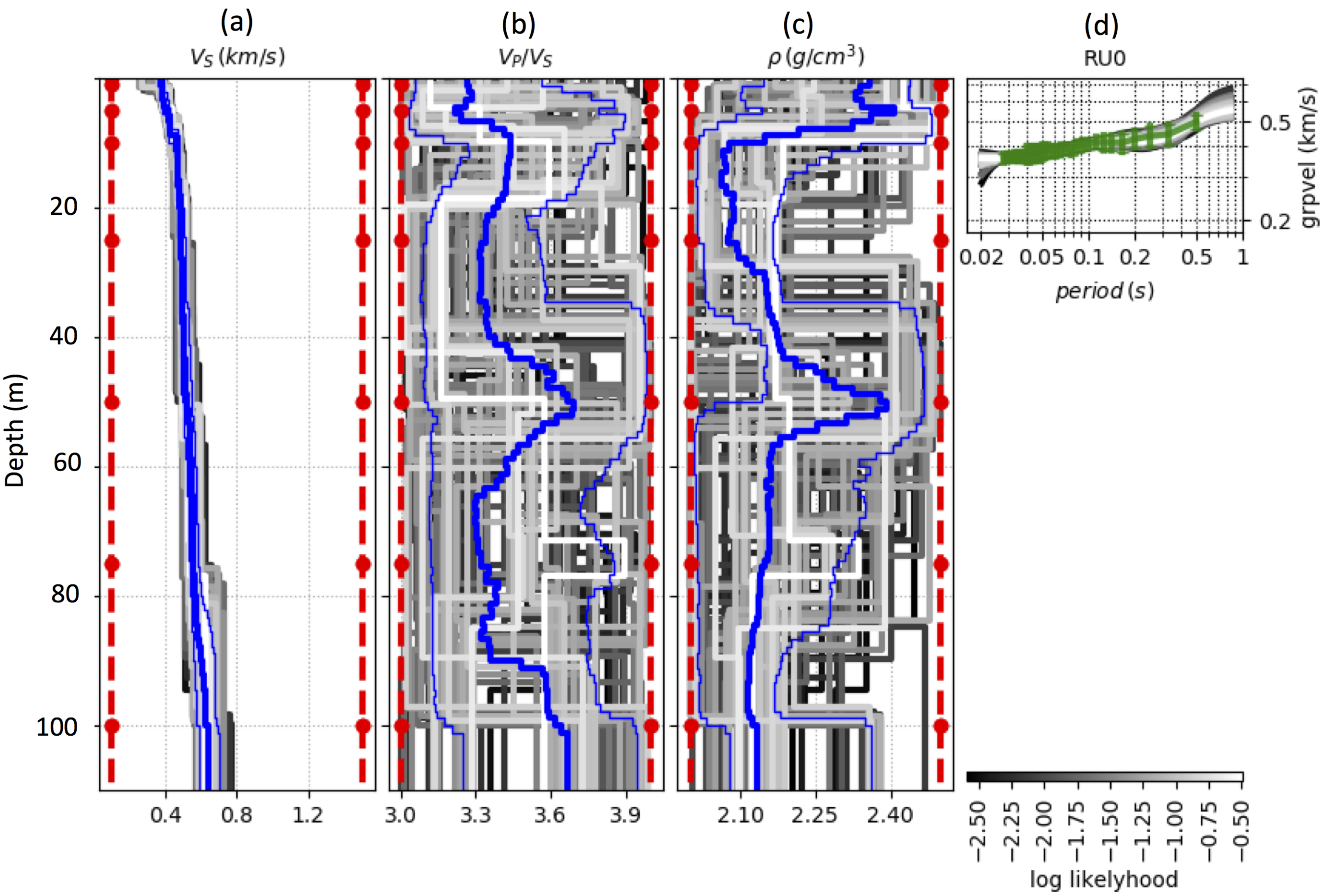

Figure 11. Example inversion results for one pixel along the DW array. The red dashed lines show the prior boundaries for the inversion and the red dots the initial location of the interfaces (see Table 1). The black and white curves show the 1000 best models for each parameter of the inversion: (a) *Vs*, (b) *Vp/Vs* ratio and (c) density. The shading corresponds to the log of the likelihood of each model (eq. 2) with better models presented in lighter colours. The blue curves show the 16, 84 (thin) and 50 per cent (thick) percentiles of the posterior distribution resampled every meter to avoid jumps in the percentiles computation. Panel (d) presents resulting synthetic dispersion curves (grey shading scale) on top of the measured dispersion data (green curve with error bars).

velocity cross-section on Fig. 10 and follows a flower shape with depth. The LVZ is located between the two major fault strands marked by solid vertical lines. All these features are better illustrated in Fig. 13(a) that shows the velocity variations relative to the mean velocity at each depth. The shallow flower structure is prominent in the top 30 m. A clear velocity contrast is observed between the SW and the NE sides of the northern fault trace.

JF array: A clear LVZ is observed at the JF array in the top 70 m and is offset to the NW from the main surface fault trace (Figs 12b and 13b), as observed to a depth of about 3.5 km with analysis of trapped waves and relative slowness computed with local earthquakes at the site (Qiu *et al.* 2017). Note that in the top 10 m the velocity is very slow with *Vs* down to ∼0.2 km s^{-1}. The velocity contrast between the NE and SW sides of the fault in the top 70 m is very clear in Fig. 13(b). The velocity contrast suggests that the main fault corresponds to the secondary fault strand marked by a dashed line and located SW of the main surface fault strand. This is consistent with the conclusion of Qiu *et al.* (2017) that the main seismogenic fault is located SW of the surface fault trace. An alternative explanation consistent with the data is that there are two fault strands at the site. Salisbury *et al.* (2012) identified surface expressions of the fault to the northwest of our JF site on Jackass Ridge and to the southeast on Rockhouse Ridge. The JF site is located in alluvium about half way in between the two ridge sites. The projection of the Jackass Ridge strand correlates with the signal between JFN2 and JFN3, while the projection of the Rockhouse strand correlates with the signal at the JF00 site (Fig. 13b).

RA array: The velocity model for the RA array presents a clear LVZ in the top 40 m that is slightly on the NE side of the fault with some flower shape with depth (Figs 12c and 13c). At shallow depth (<15 m) the LVZ is pronounced with *Vs* values between RA04 and RA10 down to 0.2 km s^{-1} (Fig. 12c). As seen in Fig. 13(c), there is a velocity contrast in the top 50 m at the edges of the LVZ around stations RA04 and RA10. This possibly indicates an ∼140 m wide trapping structure as seen at other sites in the area (e.g. Yang *et al.* 2014). The results for RA array are spatially less stable than for the other arrays and are poorly resolved below 45 m depth because of the smaller amount of data and the narrower frequency range (8–35 Hz) used at this site.

4 DISCUSSION AND CONCLUSIONS

Imaging studies based on the ambient noise field rarely use frequencies above 1 Hz, although analysis of synthetic and small-scale experiments demonstrated the possibility of obtaining high-frequency surface wave dispersions with noise cross-correlation methods (e.g. Gouédard *et al.* 2008a, 2008b). In this work we reconstructed Rayleigh waves up to 35 Hz (Figs 3–7) from the ambient

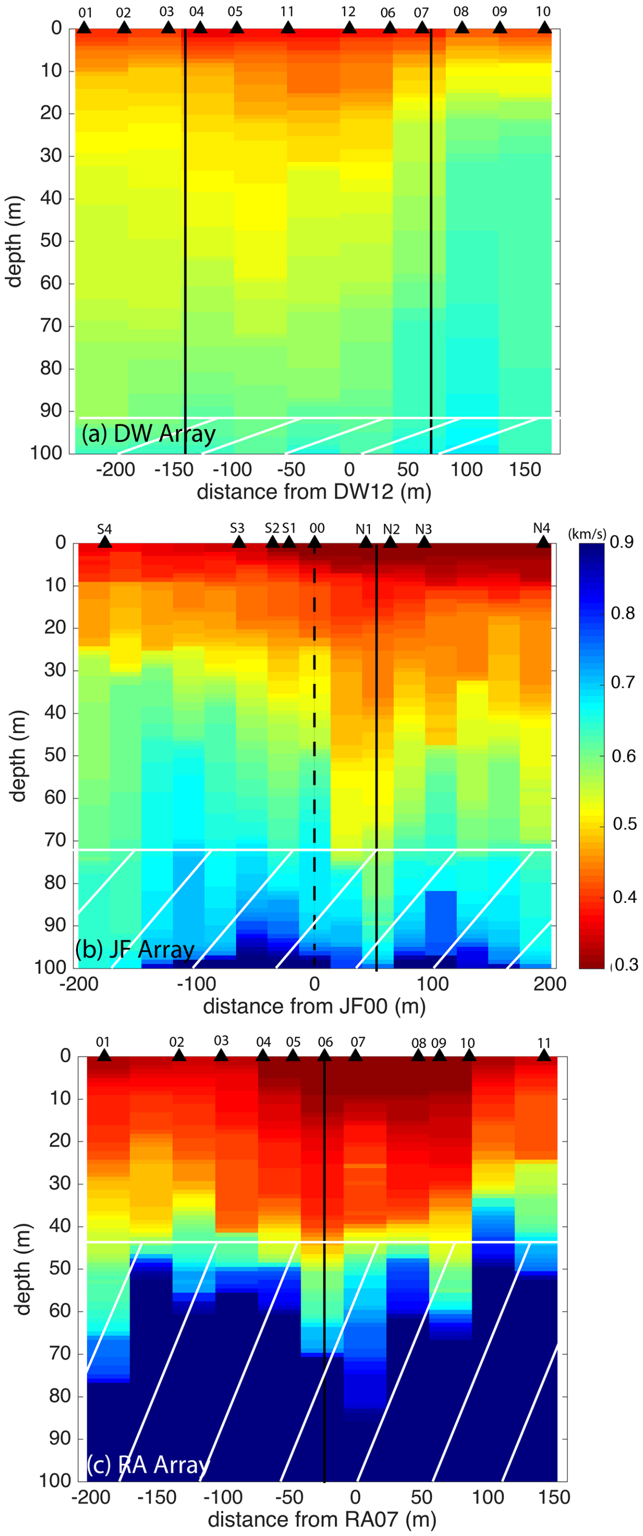

Figure 12. (a) Shear wave velocity cross-sections across (a) DW, (b) JF and (c) RA arrays. The black solid and dashed lines are vertical projections of main and secondary surface fault traces. The hatched zones mark poorly resolved depths. Note the clear low-velocity zones around surface fault traces and shallow flower structures with depths.

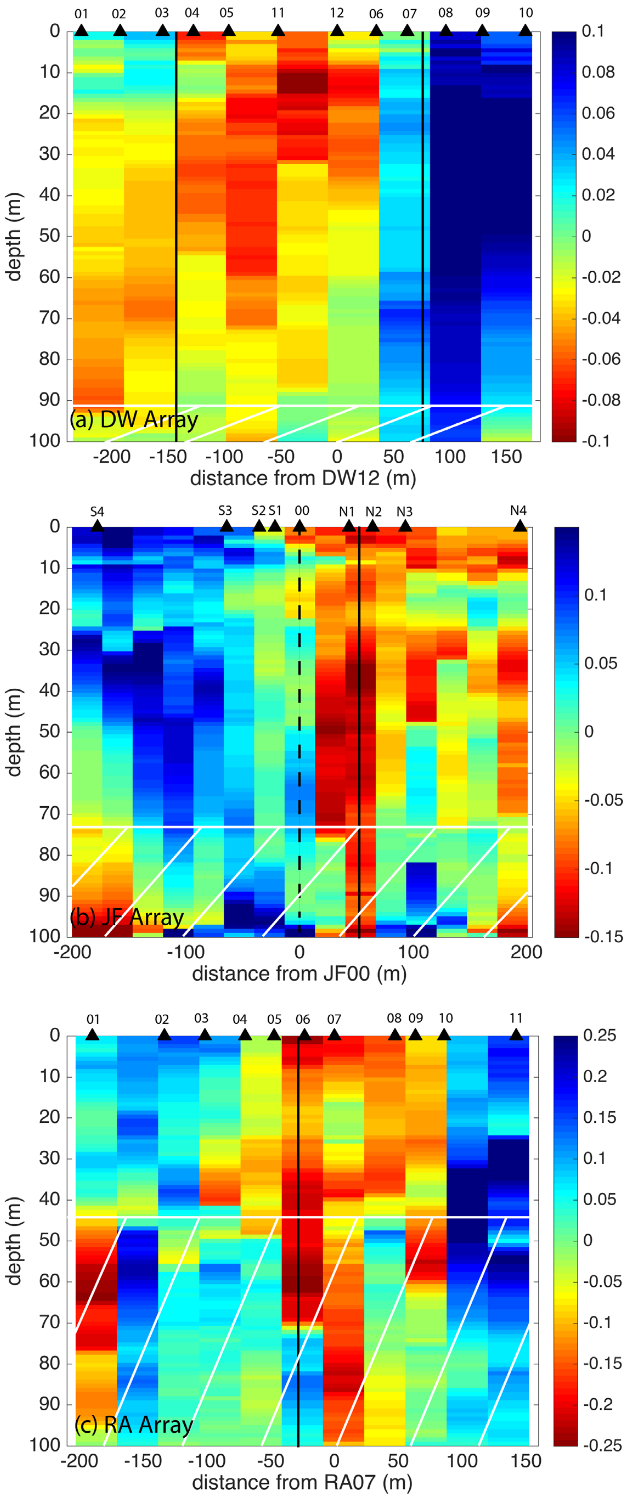

Figure 13. Similar to Fig. 12 for variations of shear wave velocities from the mean velocity at each depth.

noise field recorded by dense linear arrays at three locations across the SJFZ. This allows us to derive detailed velocity models of the subsurface structures below the arrays and helps us to bridge an observational gap between geological mapping at the surface and typical tomography studies that have little to no resolution in the top 100 m of the crust. The analysis uses passive noise-based imaging that complement active sub-surface imaging techniques.

Table 2. Major results for each array analysed.

Array	Main observations	Maximum velocity reduction ($\mathrm{km\,s^{-1}}$)	Max depth resolved depth
DW	• LVZ with a flower shape with depth marked in the top 20–30 m and located between the two major fault strands.	$0.22\ \mathrm{km\,s^{-1}}$ at 25 m depth	92m
	• A clear velocity between the SW and the NE sides of the northern fault trace	–	–
JF	• A clear LVZ is observed in the top 70 m and is offset to the NW from the main surface fault trace.	$>0.25\ \mathrm{km\,s^{-1}}$ in the first 5m	73m
	• In the top 10 m the velocity is very slow with *Vs* down to $\sim 0.2\ \mathrm{km\,s^{-1}}$.	–	–
RA	• LVZ in the top 40 m that is slightly on the NE side of the fault with some flower shape with depth.	$>0.35\ \mathrm{km\,s^{-1}}$ in the first 5m	45m
	• At shallow depth (<15 m) the LVZ is pronounced with *Vs* values between RA04 and RA10 down to $0.2\ \mathrm{km\,s^{-1}}$	–	–
	• A velocity contrast is observed in the top 50 m at the edges of the LVZ around stations RA04 and RA10.	–	–

The obtained results are similar to some previous studies of the shallow crust. Picozzi *et al.* (2008) reconstructed Rayleigh waves up to 14 Hz from high-frequency noise near Nauen, Germany, and derived a velocity model for the top 30 m across a fault that shows clear velocity contrast at shallow depths similar to our results. Hillers *et al.* (2016), Roux *et al.* (2016) and Mordret *et al.* (2018) analysed ambient noise recorded by a dense rectangular array deployed at the Sage Brush Flat site on the SJFZ (see Fig. 1 and Ben-Zion *et al.* 2015). Those studies used data up to 8 Hz to obtain high-resolution images in the top 500 m of the crust, but they lacked frequencies above 10 Hz to resolve the first tens of meters of the crust. Hillers & Campillo (2018) derived a shear wave velocity model using 2–6 Hz surface waves reconstructed from correlation of aftershock waveforms at the Landers rupture zone in California. Despite the limited frequency band analysed, they obtained a detailed *Vs* model for the top 50 m using the higher sensitivity of Love wave to the shallow structure.

An important step for surface waves imaging is to estimate the uncertainties of the dispersion maps and the shear wave velocity images. The quality of noise-based group velocity maps is mainly controlled by the network geometry and the quantity and quality of the dispersion measurements. With the linear array geometry and small number of stations used in this study, the group velocity maps (Figs 7 and 9) rely on a limited number of measurements (e.g. 18 pairs at 35 Hz and 54 pairs at 7 Hz for the DW array). To assess the dependence and variability of our group velocity maps to these minimal measurements, we perform a bootstrap analysis using randomly selected subsets with 90 per cent of the available measurements at a given frequency, and examine the consistency between the obtained group velocity maps for 1000 random selections. This is illustrated in Fig. 14 by showing the mean and standard deviation of group velocities at 15 Hz for 1000 data subsets in each cell of the DW array. The standard deviations (Fig. 14b) are about $0.012\ \mathrm{km\,s^{-1}}$; this is an order of magnitude below the overserved spatial variability and indicates stability of the obtained group velocity maps. The histograms of group velocity values (Fig. 14c) obtained for 1000 subsets in three different cells located at the edges and centre of the array also demonstrate the stability of the derived results. We note that the distributions differ mostly in the amplitude of velocity variations but the width and location of velocity anomalies remain stable. For the shear wave inversions, we used a Monte Carlo sampling to better explore the parameter space and get posterior density distributions for the many velocity models. This allows estimating how well the solution explains the data for any given position and the variability of the obtained best-fitting models (see Fig. 11). Since the frequency content is high for this study, the uncertainties increase with depth (Fig. 11a) and are significant for properties of the underlying half-space. This is highlighted on Figs 12 and 13 where the hatched zones mark the depths for which the average variability becomes similar to the *Vs* variations making any interpretations difficult. Above those depths the resulting shear wave velocity profiles, along with the position, size and amplitudes of the velocity anomalies are all well resolved.

The derived shear wave velocity models (Figs 12 and 13) show high horizontal resolution of about 50–60 m over the first 50–90 m, with prominent low-velocity zones near the surface traces of the fault for all arrays analysed. These LVZ are well marked at shallow depths with velocity reduction up to 35 per cent in the top 30 m that form in some places shallow flower structures close to the main fault (e.g. Ben-Zion & Sammis 2003). These observations provide extensions essentially up to the surface for previous imaging of prominent low-velocity zones around the arrays to depths of about 2–4 km based on analyses of internal fault zone reflections and trapped waves (Yang *et al.* 2014; Qiu *et al.* 2017; Share *et al.* 2017; Qin *et al.* 2018). These studies combined with our results indicate the existence of hierarchical damage flower structures at different sections of the SJFZ and other locations (e.g. Ben-Zion & Sammis 2003, and references therein). For all three arrays in this study, the most recent surface rupture was the 1800 November 22 M_W 7.3 event. The presence of systematic LVZ in different sections of the SJFZ indicate that the imaged damage structures reflect primarily the long-term history of the fault rather than variations within a large earthquake cycle. This inference is consistent with the observed rapid healing of coseismic velocity drops (e.g. Peng & Ben-Zion 2006; Wu *et al.* 2009; Bonilla *et al.* 2019) and the presence of damage zones close to dormant faults (e.g. Rovelli *et al.* 2002; Cochran *et al.* 2009; Hillers *et al.* 2014).

Among the three imaged sites, there is asymmetry of the LVZ in the top 100 m below the DW and JF arrays. For the DW array, the *Vs* reduction is concentrated between the two main fault strands (between stations DW03 and DW12, Figs 12a and 13a) but also shows an overall asymmetry with slower velocities of the SW side of the array as in regional tomographic images (Allam & Ben-Zion 2012; Allam *et al.* 2014; Zigone *et al.* 2015). These observations are consistent with the shape of the shallow alluvial basin location of the DW array where the deepest sediments are located on the southwest side of the array. On the other hand, the shallow LVZ below the JF array is located on the NE side of station JF00 and extends up to station JFN4 (Figs 12b and 13b). The JF array is located on the southwest side of the ∼100 m deep alluvial

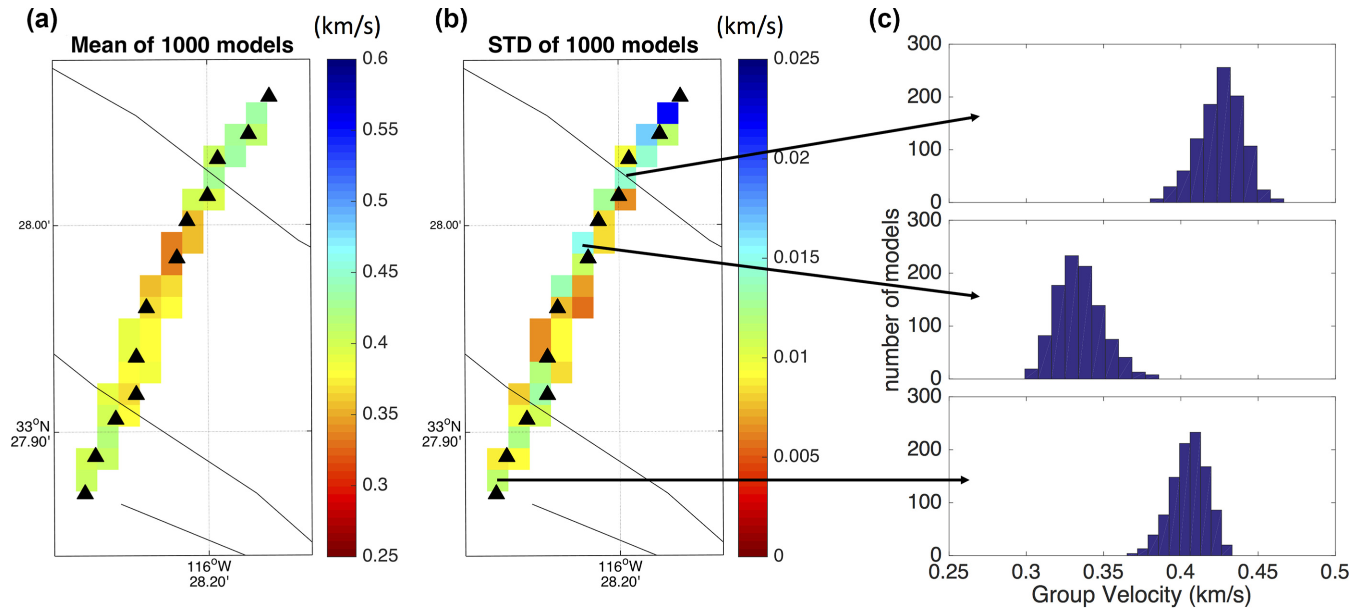

Figure 14. Bootstrap analysis results for the DW array at 15 Hz. (a) Mean of 1000 generated maps. Note the consistency with the map at 15 Hz using all measurements in Fig. 7. (b) Standard deviation of the 1000 maps. (c) Example histograms for three cells. The variations in the obtained group velocities are limited to 0.04 km s^{-1} at most. The lack of overlaps in term of absolute velocity between the histograms for cells in and outside the LVZ indicates our ability to distinguish different cells and accurately locate the position of LVZ across the fault.

basin. The LVZ indicates that the deepest part of this basin is located on the northeastern side of the JF array. The differences in the results for the three different arrays highlight the along-strike variations in the internal shallow structure reported in several studies of trapped waves (e.g. Peng *et al.* 2003; Lewis & Ben-Zion 2010).

One critical aspect of using correlation methods for imaging is the availability of continuous data over a sufficient amount of time. Typical noise interferometry with sub-Hz frequencies rely on stacking cross-correlations over several months to accurately estimate surface waves Green's functions (e.g. Shapiro *et al.* 2005; Bensen *et al.* 2007; Campillo & Roux 2015). In this study we stacked the cross-correlations over 6 months to better overcome the seasonality in the noise sources distribution (e.g. Stehly *et al.* 2006; Tanimoto *et al.* 2006; Hillers & Ben-Zion 2011). However, the high-frequency content and dense station spacing used in this work allows getting stable imaging results with data of considerably shorter duration. The shorter wavelengths sample the higher complexity of the shallow materials, which increases the scattering of the wavefield and result in shorter convergence times. This is illustrated in Fig. 15 by showing the evolution of the average SNR of all station pairs used to compute the group velocity maps as a function of the number of stacked days. The convergence rate is fast in the first 6 d with a sharp increase of the SNR (see inset in Fig. 15). The SNR then increases steadily following a typical square root of stacked time (Larose *et al.* 2007) to finally reach a plateau after about 30 stacked days. Based on Fig. 15, 90 per cent of the convergence is achieved by stacking 15 d of continuous data. Given the trend of densification of seismic networks (e.g. Lin *et al.* 2013; Ben-Zion *et al.* 2015; Nakata *et al.* 2016; Wang *et al.* 2017), the approach presented in this paper allows for rapid inexpensive imaging of the subsurface properties with temporal deployments of 30–40 d. Imaging the top crust in fault zone regions as done here can help identifying locations of active fault surfaces (including blind faults).

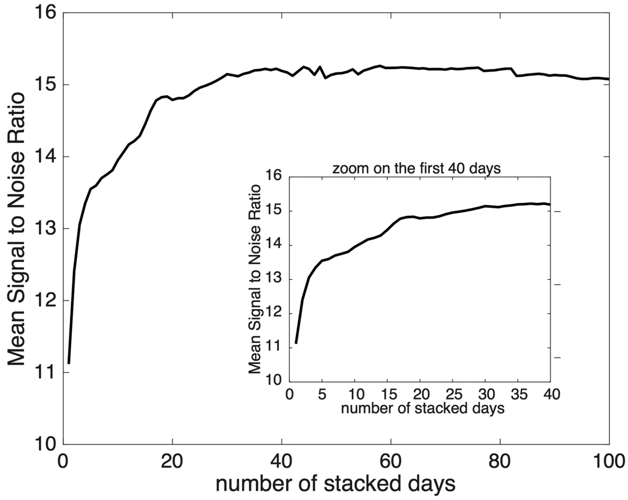

Figure 15. Mean signal-to-noise ratio of cross-correlation functions for the DW array vs. number of stacked days. The results reach 90 per cent level within 15 d. The inset shows a zoom in view for the first 40 stacked days.

ACKNOWLEDGEMENTS

We thank Xin Liu, Pierre Boué and Philippe Roux for discussions. The seismic instruments were provided by the Incorporated Research Institutions for Seismology (IRIS) through the PASSCAL Instrument Center at New Mexico Tech. The data are available through the IRIS Data Management Center. The facilities of the IRIS Consortium are supported by the National Science Foundation under Cooperative Agreement EAR-1261681 and the DOE National Nuclear Security Administration. The University of California Natural Reserve System Steele/Burnand Anza-Borrego Desert Research Center Reserve DOI: 10.21973/N3Q94F provided field support. DZ and ML acknowledge support from the LABEX ANR-11-LABX-0050-G-EAU-THERMIE-PROFONDE and from the French National Research Agency as part of the 'Investments for the Future' program. YBZ and FLV acknowledge support from the National Science Foundation (grants EAR-0908903 EAR-162061) and the Department of Energy (awards DE-SC0016520 and DE-SC0016527). MC acknowledges support from the European Research Council under the European Union Horizon 2020 research and innovation program (grant agreement no. 742335, F-IMAGE). The manuscript benefitted from constructive comments by Debi Kilb, an anonymous reviewer and Editor Egill Hauksson.

REFERENCES

Allam, A.A. & Ben-Zion, Y., 2012. Seismic velocity structures in the Southern California plate-boundary environment from double-difference tomography, *Geophys. J. Int.,* **190,** 1181–1196.

Allam, A.A., Ben-Zion, Y., Kurzon, I. & Vernon, F.L., 2014. Seismic velocity structure in the hot springs and trifurcation seismicity cluster areas of the San Jacinto fault zone from double-difference tomography, *Geophys. J. Int.,* **171,** 2993–3011.

Barmin, M.P., Ritzwoller, M.H. & Levshin, A.L., 2001. A Fast and Reliable Method for Surface Wave Tomography, *Pure appl. Geophys.,* **158** 1351–1375.

Ben-Zion, Y. & Sammis, C.G., 2003. Characterization of fault zones, *Pure appl. Geophys.,* **160,** 677–715.

Ben-Zion, Y. *et al.*, 2015. Basic data features and results from a spatially-dense seismic array on the San Jacinto fault zone, *Geophys. J. Int.,* **202,** 370–380.

Bensen, G.D., Ritzwoller, M.H., Barmin, M.P., Levshin, A.L., Lin, F.C., Moschetti, M.P., Shapiro, N.M. & Yang, Y., 2007. Processing seismic ambient noise data to obtain reliable broad-band surface wave dispersion measurements, *Geophys. J. Int.,* **169**(3), 1239–1260.

Bonilla, L.F., Guéguen, P. & Ben-Zion, Y., 2019. Monitoring co-seismic temporal changes of shallow material during strong ground motion with interferometry and autocorrelation, *Bull. seism. Soc. Am.,* **109** , 187–198.

Bonilla, L.F., Steidl, J.H., Gariel, J.C. & Archuleta, R.J., 2002. Borehole response studies at the Garner Valley downhole array, southern California, *Bull. seism. Soc. Am.,* **92**(8), 3165–3179.

Campillo, M. & Roux, P., 2015. Crust and lithospheric structure — seismic imaging and monitoring with ambient noise correlations, in *Treatise on Geophysics,* pp. 391–417, Elsevier.

Campillo, M., Singh, S., Shapiro, N., Pacheco, J. & Herrmann, R., 1996. Crustal structure south of the Mexican volcanic belt, based on group velocity dispersion, *Geofis. Int.,* **35,** 361–370.

Cochran, E.S., Li, Y.-G., Shearer, P.M., Barbot, S., Fialko, Y. & Vidale, J.E., 2009. Seismic and geodetic evidence for extensive, long-lived fault damage zones, *Geology,* **37**(4), 315–318.

Fang, H., Zhang, H., Yao, H., Allam, A., Zigone, D., Ben-Zion, Y., Thurber, C. & van der Hilst, R.D., 2016. A new three-dimensional joint inversion algorithm of body-wave and surface-wave data and its application to the Southern California Plate Boundary Region, *J. geophys. Res.,* **121,** 3557–3569.

Gallagher, K., Charvin, K., Nielsen, S., Sambridge, M. & Stephenson, J., 2009. Markov chain Monte Carlo (MCMC) sampling methods to determine optimal models, model resolution and model choice for Earth science problems, *Mar. Petrol. Geol.,* **26,** 525–535.

Goue´dard, P., Roux, P. & Campillo, M., 2008b. Small-scale seismic inversion using surface waves extracted from noise cross correlation, *J. acoust. Soc. Am.,* **123**(3), EL26, doi:10.1121/1.2838251.

Gouédard, P., Cornou, C. & Roux, P., 2008a. Phase–velocity dispersion curves and small-scale geophysics using noise correlation slantstack technique, *Geophys. J. Int.,* **172,** 971–981.

Hansen, P.C. & O'Leary, D.P., 1993. The Use of the L-curve in the regularization of discrete ill-posed problems, *SIAM J. Sci. Comput.,* **14**(6), 1487–1503.

Hauksson, E., Yang, W. & Shearer, P.M., 2012. Waveform relocated earthquake catalog for Southern California (1981 to June 2011), *Bull. seism. Soc. Am.,* **102**(5), doi:10.1785/0120120010.

Herrmann, R.B., 2013. Computer programs in seismology: An evolving tool for instruction and research, *Seismol. Res. Lett.,* **84,** 1081–1088.

Hillers, G. & Ben-Zion, Y., 2011. Seasonal variations of observed noise amplitudes at 2–18 Hz in southern California, *Geophys. J. Int.,* **184,** 860–868.

Hillers, G., Ben-Zion, Y., Landès, M. & Campillo, M., 2013. Interaction of microseisms with crustal heterogeneity: a case study from the San Jacinto fault zone area, *Geochem. Geophys. Geosyst.,* **14**(7), 2182–2197.

Hillers, G. & Campillo, M., 2018. Fault zone imaging from correlations of aftershock waveforms, *Pure appl. Geophys.,* **175,** 2643–2667.

Hillers, G., Campillo, M., Ben-Zion, Y. & Roux, P., 2014. Seismic fault zone trapped noise, *J. geophys. Res.,* **119,** doi:10.1002/2014JB011217.

Hillers, G., Campillo, M., Ben-Zion, Y. & Zigone, D., 2015. Seasonal variations of seismic velocities in the San Jacinto Fault area observed with ambient seismic noise, *Geophys. J. Int.,* **202,** 920–932.

Hillers, G., Roux, P., Campillo, M. & Ben-Zion, Y., 2016. Focal spot imaging based on zero lag cross correlation amplitude fields: application to dense array data at the San Jacinto fault zone, *J. geophys. Res.,* **121,** 8048–8067.

Inbal, A., Cristea-Platon, T., Ampuero, J.P., Hillers, G., Agnew, D. & Hough, S.E., 2018. Sources of anthropogenic noise in southern California and implications for tectonic tremor detection, *Bulletin of the Seismological Society of America,* **108,** 6, 3511–3527.

Kurzon, I., Vernon, F.L., Ben-Zion, Y. & Atkinson, G., 2014. Ground motion prediction equations in the san jacinto fault zone – significant effects of rupture directivity and fault zone amplification, *Pure appl. Geophys.,* **171,** 3045–3081.

Larose, E., Roux, P. & Campillo, M., 2007. Reconstruction of Rayleigh-Lamb dispersion spectrum based on noise obtained from an air-jet forcing, *J. acoust. Soc. Am.,* **122**(6), 3437.

Larose, E. *et al.*, 2015. Environmental seismology: what can we learn from ambient seismic noise? *J. appl. Geophys.,* **116,** 62–74.

Lecocq, T., Longuevergne, L., Pedersen, H.A., Brenguier, F. & Stammler, K., 2017. Monitoring ground water storage at mesoscale using seismic noise: 30 years of continuous observation and thermo-elastic and hydrological modeling, *Sci. Rep.,* **7,** 14241.

Lehujeur, M., Vergne, J., Schmittbuhl, J., Zigone, D., Le Chenadec, A. & Team, E., 2018. Reservoir imaging using ambient noise correlation from a dense seismic network, *J. geophys. Res.,* **123,** 6671–6686.

Levshin, A., Yanovskaya, T., Lander, A., Bukchin, B., Barmin, M., Ratnikova, L. & Its, E., 1989. *Seismic Surface Waves in a Laterally Inhomogeneous Earth,* Kluwer.

Lewis, M.A. & Ben-Zion, Y., 2010. Diversity of fault zone damage and trapping structures in the Parkfield section of the San Andreas Fault from comprehensive analysis of near fault seismograms, *Geophys. J. Int.,* **183,** 1579–1595.

Lindsey, E.O. & Fialko, Y., 2013. Geodetic slip rates in the southern San Andreas Fault system: effects of elastic heterogeneity and fault geometry, *J. geophys. Res.,* **118,** 689–697.

Lin, F.-C., Li, D., Clayton, R.W. & Hollis, D., 2013. High-resolution 3D shallow crustal structure in Long Beach, California: application of ambient noise tomography on a dense seismic array, *Geophysics,* **78,** Q45–Q56.

Lin, G., Shearer, P.M. & Hauksson, E., 2007. Applying a three-dimensional velocity model, waveform cross correlation, and cluster analysis to locate southern California seismicity from 1981 to 2005, *J. geophys. Res.,* **112,** B12309, doi:10.1029/2007JB004986.

Maraschini, M. & Foti, S., 2010. A Monte Carlo multimodal inversion of surface waves, *Geophys. J. Int.,* **182**(3), 1557–1566.

Mavko, G., Mukerji, T. & Dvorkin, J., 2009. *The Rock Physics Handbook: Tools for Seismic Analysis of Porous Media. Cambridge,* Cambridge University Press, doi:10.1017/CBO9780511626753.

Meng, H. & Ben-Zion, Y., 2018. Characteristics of airplanes and helicopters recorded by a dense seismic array near Anza California, *J. geophys. Res.,* **123,** 4783–4797.

Mordret, A., Roux, P., Boué, P. & Ben-Zion, Y., 2018. Shallow 3-D structure of the San Jacinto Fault zone revealed from ambient noise imaging with a dense seismic array, *Geophys. J. Int.,* **216,** 896–905.

Nakata, N., Boué, P., Brenguier, F., Roux, P., Ferrazzini, V. & Campillo, M., 2016. Body and surface wave reconstruction from seismic noise correlations between arrays at Piton de la Fournaise volcano, *Geophys. Res. Lett.,* **43,** 1047–1054.

Peng, Z. & Ben-Zion, Y., 2006. Temporal changes of shallow seismic velocity around the Karadere-Duzce branch of the north Anatolian fault and strong ground motion, *Pure appl. Geophys.,* **163,** 567–600.

Peng, Z., Ben-Zion, Y., Michael, A.J. & Zhu, L., 2003. Quantitative analysis of seismic trapped waves in the rupture zone of the 1992 Landers, California earthquake: Evidence for a shallow trapping structure, *Geophys. J. Int.,* **155,** 1021–1041.

Picozzi, M., Parolai, S., Bindi, D. & Strollo, A., 2008. Characterization of shallow geology by high-frequency seismic noise tomography, *Geophys. J. Int.,* **176**(1), 164–174.

Poli, P., Pedersen, H.A. & Campillo, M., the POLENET/LAPNET Working Group, 2012. Noise directivity and group velocity tomography in a region with small velocity contrasts: the northern Baltic Shield, *Geophys. J. Int.,* **192,** 413–424.

Qin, L., Ben-Zion, Y., Qiu, H., Share, P.-E., Ross, Z.E. & Vernon, F.L., 2018. Internal structure of the San Jacinto fault zone in the trifurcation area southeast of Anza, California, from data of dense seismic arrays, *Geophys. J. Int.,* **213,** 98–114.

Qiu, H., Ben-Zion, Y., Ross, Z.E., Share, P.-E. & Vernon, F.L., 2017. Internal structure of the San Jacinto fault zone at Jackass Flat from data recorded by a dense linear array, *Geophys. J. Int.,* **209,** 1369–1388.

Rockwell, T.K., Dawson, T.E., Ben-Horton, J.Y. & Seitz, G., 2015. A 21 event, 4,000-year history of surface ruptures in the Anza Seismic Gap, San Jacinto fault and implications for long term earthquake production on a major plate boundary fault, *Pure appl. Geophys.,* **172**(5), 1143–1165.

Ross, Z.E., Hauksson, E. & Ben-Zion, Y., 2017. Abundant off-fault seismicity and orthogonal structures in the San Jacinto fault zone, *Sci. Adv.,* **3,** e1601946, doi: 10.1126/sciadv.1601946.

Roux, P., Moreau, L., Lecointre, A., Hillers, G., Campillo, M., Ben-Zion, Y., Zigone, D. & Vernon, F., 2016. A methodological approach toward high-resolution surface wave imaging of the San Jacinto Fault Zone using ambient-noise recordings at a spatially dense array, *Geophys. J. Int.,* **206,** 980–992.

Rovelli, A., Caserta, A., Marra, F. & Ruggiero, V., 2002. Can seismic waves be trapped inside an inactive fault zone? The case study of Nocera Umbra, central Italy, *Bull. seism. Soc. Am.,* **92,** 2217–2232.

Salisbury, J.B., Rockwell, T.K. & Buga, M.T., 2017. Paleoseismic evidence for the 21 April 1918 M_W 6.9 surface rupture of the northern Clark Strand of the central San Jacinto Fault, California, *Bull. seism. Soc. Am.,* **107**(2): 1027–1032.

Salisbury, J.B., Rockwell, T.K., Middletion, T.J. & Hudnut, K.W., 2012. LiDAR and field observations of slip distribution for the most recent surface ruptures along the central San Jacinto Fault, *Bull. seism. Soc. Am.,* **102,** 598–619.

Sambridge, M. & Mosegaard, K., 2002. Monte Carlo methods in geophysical inverse problems, *Rev. Geophys.,* **40**(3), 3–1-3-29.

Shapiro, N.M., Campillo, M., Paul, A., Singh, S.K., Jongmans, D. & Sanchez-Sesma, F.J., 1997. Surface-wave propagation across the Mexican Volcanic Belt and the origin of the long-period seismic-wave amplification in the Valley of Mexico, *Geophys. J. Int.,* **128,** 151–166.

Shapiro, N.M., Campillo, M., Stehly, L. & Ritzwoller, M.H., 2005. High resolution surface-wave tomography from ambient seismic noise, *Science,* **29,** 1615–1617.

Shapiro, N.M. & Ritzwoller, M.H., 2002. Monte-Carlo inversion for a global shear-velocity model of the crust and upper mantle, *Geophys. J. Int.,* **151**(1), 88–105.

Share, P.-E., Ben-Zion, Y., Ross, Z.E., Qiu, H. & Vernon, F.L., 2017. Internal structure of the San Jacinto fault zone at Blackburn Saddle from seismic data of a dense linear array, *Geophys. J. Int.,* **210,** 819–832.

Socco, L.V. & Boiero, D., 2008. Improved Monte Carlo inversion of surface wave data, *Geophys. Prospect.,* **56**(3), 357–371.

Stehly, L., Campillo, M. & Shapiro, N.M., 2006. A study for the seismic noise from its long-range correlation properties, *J. geophys. Res.,* **111,** B10306, doi:10.1029/2005JB004237.

Stehly, L., Fry, B., Campillo, M., Shapiro, N.M., Guilbert, J., Boschi, L. & Giardini, D., 2009. Tomography of the Alpine region from observations of seismic ambient noise, *Geophys. J. Int.,* **178**(1), 338–350.

Tanimoto, T., Ishimaru, S. & Alvizuri, C., 2006. Seasonality of particle motion of microseisms, *Geophys. J. Int.,* **166,** 253–266.

Tarantola, A., 2005. *Inverse Problem Theory & Methods for Model Parameter Estimation,* SIAM, doi:10.1137/1.9780898717921.

Verbeke, J., Boschi, L., Stehly, L., Kissling, E. & Michelini, A., 2012. High-resolution Rayleigh-wave velocity maps of central Europe from a dense ambient-noise data set, *Geophys. J. Int.,* **188**(3), 1173–1187.

Wang, Y., Lin, F.-C., Schmandt, B. & Farrell, J., 2017. Ambient noise tomography across Mount St. Helens using a dense seismic array, *J. geophys. Res.,* **122,** 2016JB013769, doi:10.1002/2016JB013769.

Whearty, J.J., Rockwell, T.K. & Girty, G.H., 2017. Incipient pulverization at shallow burial depths along the San Jacinto Fault, Southern California, in *Fault Zone Dynamic Processes: Evolution of Fault Properties During Seismic Rupture,* Geophysical Monograph Series, vol. **227,** Thomas, M. Y., Mitchell, T. M. & Bhat, H. S., eds, Wiley, doi:10.1002/9781119156895.

Wu, C., Peng, Z. & Ben-Zion, Y., 2009. Non-linearity and temporal changes of fault zone site response associated with strong ground motion, *Geophys. J. Int.,* **176,** 265–278.

Xia, J., Miller, R. & Park, C., 1999. Estimation of near-surface shear-wave velocity by inversion of Rayleigh waves, *Geophysics,* **64,** 691–700.

Yang, H., Li, Z., Peng, Z., Ben-Zion, Y. & Vernon, F., 2014. Low-velocity zones along the San Jacinto Fault, Southern California, from body waves recorded in dense linear arrays, *J. geophys. Res.,* **119,** 8976–8990.

Zigone, D., Ben-Zion, Y., Campillo, M. & Roux, P., 2015. Seismic tomography of the Southern California plate boundary region from noise-based Rayleigh and love waves, *Pure appl. Geophys.,* **172,** 1007–1032.

SUPPORTING INFORMATION

Supplementary data are available at *GJI* online.

Figure S1. Variance reduction as a function of the four different parameters used in the inversion (L-curve analysis) for DW at 20 Hz: (a) damping factor α, (b) β, (c) λ and (d) correlation length σ. The chosen parameters are indicated by the red dots.

Please note: Oxford University Press is not responsible for the content or functionality of any supporting materials supplied by the authors. Any queries (other than missing material) should be directed to the corresponding author for the paper.